

See discussions, stats, and author profiles for this publication at: <https://www.researchgate.net/publication/26880502>

# Theoretical Characterization of an Atmospheric Pressure Glow Discharge Used for Analytical Spectrometry

ARTICLE *in* ANALYTICAL CHEMISTRY · OCTOBER 2009

Impact Factor: 5.64 · DOI: 10.1021/ac9017742 · Source: PubMed

---

CITATIONS

13

---

READS

60

4 AUTHORS, INCLUDING:



**Annemie Bogaerts**

University of Antwerp

465 PUBLICATIONS 7,270 CITATIONS

SEE PROFILE

# Theoretical Characterization of an Atmospheric Pressure Glow Discharge Used for Analytical Spectrometry

Tom Martens,<sup>†</sup> Diana Mihailova,<sup>‡</sup> Jan van Dijk,<sup>‡</sup> and Annemie Bogaerts<sup>\*†</sup>

Research Group PLASMANET, Department of Chemistry, University of Antwerp, Universiteitsplein 1, B-2610 Wilrijk, Belgium, and Research Group Elementary Processes in Gas Discharges, Department of Applied Physics, Eindhoven University of Technology, P.O. Box 513, 5600 MB, Eindhoven, The Netherlands

We have investigated the plasma processes in an atmospheric pressure glow discharge (APGD) in He used for analytical spectrometry by means of fluid and Monte Carlo (MC) simulations. Typical results include the potential and electric field distributions in the plasma, the density profiles of the various plasma species throughout the discharge, the mean electron energy, as well as the rates of the various collision processes in the plasma, and the relative importance of the different production and loss rates for the various species. The similarities and differences with low-pressure glow discharges are discussed. The main differences are a very small cathode dark space region and a large positive column as well as the dominant role of molecular ions. Some characteristic features of the APGD, such as the occurrence of the different spatial zones in the discharge, are illustrated, with links to experimental observations.

Glow discharges (GDs) at reduced pressure (typically 50–500 Pa) are widely used for the analysis of (mainly solid) materials.<sup>1,2</sup> In recent years, however, there is increased interest for the analysis of liquids and gaseous samples. For these applications, GDs operating at atmospheric pressure (so-called APGDs) appear to be particularly useful. Various groups have proposed different plasma designs, and several review papers have been published on these APGDs and microplasmas, not only for analytical applications (e.g., refs 3–6) but also for materials processing, environmental, and biomedical applications.<sup>7,8</sup> The miniaturized direct current (dc) GDs (e.g., refs 9–13) are based on similarity

laws, which state that the gap between the electrodes must be reduced when pressure is increased. They have been applied for instance for dc microplasma “on a chip” gas chromatography.<sup>10–13</sup> Also the use of microhollow cathode dc discharges (MHCDs) has been investigated for analytical applications.<sup>14</sup> Besides dc discharges, radiofrequency (rf) powering schemes have also been applied, such as in ref 15. This rf powering is often combined with dielectric barrier materials at the surface of one or both electrodes, i.e., so-called dielectric barrier discharges (DBDs), which can operate both at atmospheric pressure and reduced pressure.<sup>16,17</sup>

Hieftje and co-workers have been particularly active in recent years in developing new designs for APGDs. The so-called annular GD,<sup>18</sup> maintained in atmospheric pressure He between a tubular cathode and a rod-shaped anode, was developed for solution analysis. For gaseous analysis, the Hieftje group reported on a versatile direct current (dc) APGD in He interfaced with a time-of-flight mass spectrometer.<sup>19,20</sup> A very stable APGD could be maintained between a rod-shaped cathode and anode, separated by 1 cm distance. The anode was characterized by a conical end, which appeared to help in stabilizing the discharge in the high-pressure regime. This APGD was characterized in ref 20 by means of electrical and spectroscopic measurements. It could be deduced from the presence of He<sup>+</sup> ions in the mass spectrum that a

\* To whom correspondence should be addressed. E-mail: annemie.bogaerts@ua.ac.be.

<sup>†</sup> University of Antwerp.

<sup>‡</sup> Eindhoven University of Technology.

- (1) Marcus, R. K.; Broekaert, J. A. C., Eds. *Glow Discharge Plasmas in Analytical Spectrometry*; John Wiley and Sons, Ltd.: Chichester, U.K., 2003.
- (2) Jakubowski, N.; Bogaerts, A.; Hoffmann, V. Glow Discharges in Emission and Mass Spectrometry. In *Atomic Spectroscopy in Elemental Analysis*; Cullen, M., Ed.; Blackwell: Sheffield, U.K., 2003.
- (3) Broekaert, J. A. C. *Anal. Bioanal. Chem.* **2002**, *374*, 182–187.
- (4) Franzke, J.; Kunze, K.; Miclea, M.; Niemax, K. *J. Anal. At. Spectrom.* **2003**, *18*, 802–807.
- (5) Karanassios, V. *Spectrochim. Acta, Part B* **2004**, *59*, 909–928.
- (6) Hopwood, J.; Iza, F. *J. Anal. At. Spectrom.* **2004**, *19*, 1145–1150.
- (7) Massines, F. *J. Phys. D: Appl. Phys.* **2005**, *38*, 505–575 (Special Issue on Atmospheric Pressure Non-Thermal Plasmas for Processing and Other Applications).

- (8) Tander, C.; Tixier, C.; Tristant, P.; Desmaison, J.; Leprince, Ph. *Spectrochim. Acta, Part B* **2006**, *61*, 2–30.
- (9) Layman, L. R.; Hieftje, G. M. *Anal. Chem.* **1975**, *47*, 194–202.
- (10) Eijkel, J. C. T.; Stoeri, H.; Manz, A. *J. Anal. At. Spectrom.* **2000**, *15*, 297–300.
- (11) Bessoth, F. G.; Naji, O. P.; Eijkel, J. C. T.; Manz, A. *J. Anal. At. Spectrom.* **2002**, *17*, 794–799.
- (12) Eijkel, J. C. T.; Stoeri, H.; Manz, A. *Anal. Chem.* **2000**, *72*, 2547–2552.
- (13) Kim, H. J.; Woo, Y. A.; Kang, J. S.; Anderson, S. A.; Piepmeyer, E. H. *Mikrochim. Acta* **2000**, *134*, 1–7.
- (14) Miclea, M.; Kunze, K.; Heitmann, U.; Florek, S.; Franzke, J.; Niemax, K. *J. Phys. D: Appl. Phys.* **2005**, *48*, 1709–1715.
- (15) Sturgeon, R. E.; Luong, V. T.; Willie, S. N.; Marcus, R. K. *Spectrochim. Acta, Part B* **1993**, *48*, 893–908.
- (16) Zhu, Z.; Zhang, S.; Xue, J.; Zhang, X. *Spectrochim. Acta, Part B* **2006**, *61*, 916–921.
- (17) Miclea, M.; Kunze, K.; Musa, G.; Franzke, J.; Niemax, K. *Spectrochim. Acta, Part B* **2001**, *56*, 37–43.
- (18) Webb, M. R.; Andrade, F. J.; Hieftje, G. M. *J. Anal. At. Spectrom.* **2007**, *22*, 775–782.
- (19) Wetzel, W. C.; Andrade, F. J.; Broekaert, J. A. C.; Hieftje, G. M. *J. Anal. At. Spectrom.* **2006**, *21*, 750–756.
- (20) Andrade, F. J.; Wetzel, W. C.; Chan, G. C.-Y.; Webb, M. R.; Gamez, G.; Ray, S. J.; Hieftje, G. M. *J. Anal. At. Spectrom.* **2006**, *21*, 1175–1184.

significant amount of energy was available for the ionization of gaseous analyte species. When this detection system is coupled with hydride generation, the analytical performance becomes comparable to that of an inductively coupled plasma source.<sup>19</sup>

This APGD has also been modified by Andrade et al.<sup>21,22</sup> to be used in the flowing afterglow mode as a chemical ionization source for organic mass spectrometry: the ions and excited species generated by the APGD, such as the He\* metastable atoms, are transported outside the discharge chamber. They create a high flux of reagent ions, such as protonated water clusters, nitrogen dimer ions, and oxygen ions, which can efficiently ionize analyte species that are placed within the afterglow region. This so-called flowing atmospheric pressure afterglow (FAPA) source has been applied both for the ionization of compounds in the gas phase<sup>21</sup> as well as for desorption–ionization for the direct analysis of solid compounds.<sup>22</sup>

Other plasma sources, besides FAPA, that are developed in recent years for ambient desorption–ionization mass spectrometry (ADI-MS) or simply ambient mass spectrometry (AMS) include the direct analysis in real time (DART),<sup>23</sup> dielectric barrier discharge ionization (DBDI),<sup>24</sup> and plasma-assisted desorption/ionization (PADi).<sup>25</sup> In general, all these techniques allow the direct desorption/ionization of a broad range of samples, with no sample preparation.<sup>26</sup> They produce simple mass spectra with little or no fragmentation. They are attractive because of high sample throughput, ease of use, low initial costs, and low operating expense.<sup>26</sup> In ref 27, Shelley et al. made a detailed comparison between the FAPA and DART. Although both sources appear to be similar at first glance, they seem to operate in different regimes, i.e., corona-to-glow transition for DART and glow-to-arc transition for the FAPA source.

Furthermore, Shelley et al. coupled the FAPA source with laser ablation to be used for molecular mass spectral imaging,<sup>28</sup> and Schilling et al. applied it for elemental analysis through hydride generation.<sup>26</sup> This study demonstrated the ability to use an ambient mass spectrometry source, commonly used for molecular analysis, for the detection of gas phase elemental species with the possibility of performing speciation by coupling with a separation technique.

To optimize the applications of these APGDs, a thorough characterization of the GD plasma is desirable. This can be done by experiments, such as electrical characterization and optical emission spectrometry, as is demonstrated in ref 20. Other measuring techniques that can in principle be applied include

Langmuir probes (which give information on electron and ion densities, the electron temperature and electron energy distribution, and the plasma potential) as well as laser absorption or scattering techniques (which can provide information on species densities or the electron and gas temperature). However, because of the small dimensions, measuring inside the plasma is not always practical. Moreover, measuring the number densities of the various species present in the plasma is not so straightforward. In this respect, computer modeling can be very useful.

There exist several papers in the plasma physics literature about modeling APGDs.<sup>29–33</sup> Most commonly, fluid approaches are applied,<sup>29–32</sup> although the particle-in-cell Monte Carlo technique has been used as well.<sup>33</sup> Most studies concern DBDs because of their increasing applications in materials processing, environmental, and biomedical applications.<sup>34,35</sup> We have also studied a reduced pressure DBD used as a microchip source for analytical spectrometry,<sup>36</sup> and we have investigated the effect of pressure in the discharge.<sup>37</sup> Shi and Kong have published a simple hybrid model for a dc APGD in He used for material processing applications.<sup>38</sup> The model was based on a so-called kinetic description in the cathode fall region and a hydrodynamic model in the rest of the discharge. The calculation results confirmed many characteristics of GDs, and correlations were made with low-pressure GDs, in terms of the manifestation of the structural characteristics, especially in the formation of the nonequilibrium cathode fall and a nearly neutral positive column.

In the past decades, we have developed comprehensive models to describe the plasma behavior of reduced pressure GDs used for analytical spectrometry (e.g., refs 39–41). However, these insights cannot directly be transferred to APGDs because of the different operating conditions. Indeed, the high pressure gives rise to more collisions and also to other types of collisions (such as three-body collisions, formation of molecular ions, etc). Moreover, the structure of the GD is also different in both cases, i.e., at the low pressure case, the positive column region is typically absent, whereas this region can become the dominant one at atmospheric pressure. This was very nicely demonstrated in ref 20. Therefore, the present paper focuses on modeling efforts for an APGD used for spectrochemical analysis. As a case study, the APGD described in refs 19 and 20 is investigated, but the results can be transferred also to other APGD designs.

- (21) Andrade, F. J.; Shelley, J. T.; Wetzel, W. C.; Webb, M. R.; Gamez, G.; Ray, S. J.; Hieftje, G. M. *Anal. Chem.* **2008**, *80*, 2646–2653.
- (22) Andrade, F. J.; Shelley, J. T.; Wetzel, W. C.; Webb, M. R.; Gamez, G.; Ray, S. J.; Hieftje, G. M. *Anal. Chem.* **2008**, *80*, 2654–2663.
- (23) Cody, R. B.; Laramée, J. A.; Durst, H. D. *Anal. Chem.* **2005**, *77*, 2297–2302.
- (24) Na, N.; Zhao, M. X.; Zhang, S. C.; Yang, C. D.; Zhang, X. R. *J. Am. Soc. Mass Spectrom.* **2007**, *18*, 1859–1862.
- (25) Ratcliffe, L. V.; Rutten, F. J. M.; Barrett, D. A.; Whitmore, T.; Seymour, D.; Greenwood, C.; Aranda-Gonzalvo, Y.; Robinson, S.; McCoustrat, M. *Anal. Chem.* **2007**, *79*, 6094–6101.
- (26) Schilling, G. D.; Shelley, J. T.; Broekaert, J. A. C.; Sperline, R. P.; Denton, M. B.; Barinaga, C. J.; Koppenaal, D. W.; Hieftje, G. M. *J. Anal. At. Spectrom.* **2009**, *24*, 34–40.
- (27) Shelley, J. T.; Wiley, J. S.; Chan, G. C. Y.; Schilling, G. D.; Ray, S. J.; Hieftje, G. M. *J. Am. Soc. Mass Spectrom.* **2009**, *20*, 837–844.
- (28) Shelley, J. T.; Ray, S. J.; Hieftje, G. M. *Anal. Chem.* **2008**, *80*, 8308–8313.

- (29) Massines, F.; Rabehi, A.; Decomps, P.; Gadri, R. B.; Segur, P.; Mayoux, C. *J. Appl. Phys.* **1998**, *83*, 2950–2957.
- (30) Golubovskii, Y. B.; Maiorov, V. A.; Behnke, J.; Behnke, J. F. *J. Phys. D: Appl. Phys.* **2003**, *36*, 39–49.
- (31) Farouk, T.; Farouk, B.; Staack, D.; Gutsol, A.; Fridman, A. *Plasma Sources Sci. Technol.* **2006**, *15*, 676–688.
- (32) Wang, Q.; Economou, D. J.; Donnelly, V. M. *J. Appl. Phys.* **2006**, *100*, 023301.
- (33) Choi, J.; Iza, F.; Lee, J. K.; Ryu, C. M. *IEEE Trans. Plasma Sci.* **2007**, *35*, 1274–1278.
- (34) Kogelschatz, U. *Plasma Chem. Plasma Process.* **2003**, *23*, 1–46.
- (35) Wagner, H. E.; Brandenburg, R.; Kozlov, K. V.; Sonnenfeld, A.; Michel, P.; Behnke, J. F. *Vacuum* **2003**, 417–436.
- (36) Martens, T.; Bogaerts, A.; Brok, W.; van Dijk, J. *Anal. Bioanal. Chem.* **2007**, *388*, 1583–1594.
- (37) Martens, T.; Bogaerts, A.; Brok, W. J. M.; van der Mullen, J. J. A. M. *J. Anal. At. Spectrom.* **2007**, *22*, 1033–1042.
- (38) Shi, J. J.; Kong, M. G. *J. Appl. Phys.* **2003**, *94*, 5504–5513.
- (39) Bogaerts, A.; Gijbels, R. *Anal. Chem.* **1997**, *69*, A719–A727.
- (40) Bogaerts, A.; Gijbels, R. *Spectrochim. Acta, Part B* **1998**, *53*, 437–462.
- (41) Bogaerts, A. *J. Anal. At. Spectrom.* **2007**, *22*, 13–40.

**Table 1. Reactions Included in the Model With Their Rate Coefficients<sup>a</sup>**

no. of reaction	reaction	rate coefficient (or cross section)	ref
1	$e^- + \text{He} \rightarrow e^- + \text{He}_m^*$	$\sigma(\varepsilon)$	61
2	$e^- + \text{He} \rightarrow 2e^- + \text{He}^+$	$\sigma(\varepsilon)$	61
3	$e^- + \text{He}_m^* \rightarrow 2e^- + \text{He}^+$	$\sigma(\varepsilon)$	61
4	$2e^- + \text{He}^+ \rightarrow e^- + \text{He}$	$3 \times 10^{-20} (T_g/T_e)^4 \text{ cm}^6 \text{ s}^{-1}$	69
5	$2e^- + \text{He}^+ \rightarrow e^- + \text{He}_m^*$	$3 \times 10^{-20} (T_g/T_e)^4 \text{ cm}^6 \text{ s}^{-1}$	69
6	$e^- + \text{He}_2^+ \rightarrow \text{He}_m^* + \text{He}$	$8.9 \times 10^{-9} (T_g/T_e)^{1.5} \text{ cm}^3 \text{ s}^{-1}$	30
7	$e^- + \text{N}_2^+ \rightarrow \text{N} + \text{N} \rightarrow \text{N}_2$	$4.8 \times 10^{-7} (T_g/T_e)^{0.5} \text{ cm}^3 \text{ s}^{-1}$	30
8	$e^- + \text{N}_4^+ \rightarrow \text{N}_2 + \text{N}_2$	$2 \times 10^{-6} (T_g/T_e)^{0.5} \text{ cm}^3 \text{ s}^{-1}$	70
9	$\text{He}^+ + 2\text{He} \rightarrow \text{He}_2^+ + \text{He}$	$1.1 \times 10^{-31} \text{ cm}^6 \text{ s}^{-1}$	30
10	$\text{He}_2^+ + \text{N}_2 \rightarrow \text{He}_2^* + \text{N}_2^+$	$1.4 \times 10^{-9} \text{ cm}^3 \text{ s}^{-1}$	30
11	$\text{N}_2^+ + 2\text{N}_2 \rightarrow \text{N}_4^+$	$1.9 \times 10^{-29} \text{ cm}^6 \text{ s}^{-1}$	71
12	$\text{N}_2^+ + \text{N}_2 + \text{He} \rightarrow \text{N}_4^+ + \text{He}$	$1.9 \times 10^{-29} \text{ cm}^6 \text{ s}^{-1}$	71
13	$\text{N}_4^+ + \text{N}_2 \rightarrow \text{N}_2^+ + 2\text{N}_2$	$2.5 \times 10^{-15} \text{ cm}^3 \text{ s}^{-1}$	70
14	$\text{N}_4^+ + \text{He} \rightarrow \text{N}_2^+ + \text{N}_2 + \text{He}$	$2.5 \times 10^{-15} \text{ cm}^3 \text{ s}^{-1}$	70
15	$\text{He}_m^* + 2\text{He} \rightarrow \text{He}_2^* + \text{He}$	$2 \times 10^{-34} \text{ cm}^6 \text{ s}^{-1}$	30
16	$\text{He}_m^* + \text{He}_m^* \rightarrow \text{He}^+ + \text{He} + e^-$	$1.5 \times 10^{-9} \text{ cm}^3 \text{ s}^{-1}$	69
17	$\text{He}_m^* + \text{He}_m^* \rightarrow \text{He}_2^+ + e^-$	$1.5 \times 10^{-9} \text{ cm}^3 \text{ s}^{-1}$	30
18	$\text{He}_m^* + \text{N}_2 \rightarrow \text{He} + \text{N}_2^+ + e^-$	$5 \times 10^{-11} \text{ cm}^3 \text{ s}^{-1}$	30
19	$\text{He}_2^* + \text{M} \rightarrow 2\text{He} + \text{M}$	$10^{-4} \text{ s}^{-1}$	30
20	$\text{He}_2^* + \text{He}_2^* \rightarrow \text{He}_2^+ + 2\text{He} + e^-$	$1.5 \times 10^{-9} \text{ cm}^3 \text{ s}^{-1}$	30
21	$\text{He}_2^* + \text{N}_2 \rightarrow 2\text{He} + \text{N}_2^+ + e^-$	$3 \times 10^{-11} \text{ cm}^3 \text{ s}^{-1}$	30

<sup>a</sup> The electron impact reactions are described with energy-dependent cross sections. The last column gives the references where the rate coefficients and cross sections are adopted from. In the MC model, the electron-impact reactions (eqs 1–3) are included as well as electron impact excitation of the N<sub>2</sub> impurities to the lowest rotational and vibrational levels.

## DESCRIPTION OF THE MODELING WORK

**General Overview: Models Used and Species and Reactions Considered in the Model.** To describe the APGD, we make use of a fluid model, as well as Monte Carlo (MC) simulations. Fluid modeling is particularly useful for describing plasmas at atmospheric pressure. Indeed, at high pressure, the plasma species have high number densities and they take part in many collisions and to describe these species and all their collisions with a kinetic model (e.g., MC simulations) would be very time-consuming. Moreover, at high pressure, the plasma species can lose much of their energy by collisions, so that a fluid approach is generally acceptable, because the gain of energy by the electric field is more or less balanced by the loss of energy due to collisions. However, this is not really true for the electrons because they gain more energy from the electric field than they lose by collisions. Therefore, we have also developed a MC model to describe the behavior of the electrons in the APGD.

The APGD under study is the one described in refs 19 and 20. It operates at 1 atm helium (99.999% purity). Because some nitrogen peaks are detected in the UV–vis emission spectrum,<sup>20</sup> we have included 10 ppm nitrogen in the calculations. The species included in the model comprise the background gases He and N<sub>2</sub>, the ions He<sup>+</sup>, He<sub>2</sub><sup>+</sup>, N<sub>2</sub><sup>+</sup>, and N<sub>4</sub><sup>+</sup>, the metastable He atoms (He<sub>m</sub><sup>\*</sup>), and the He excimers (He<sub>2</sub><sup>\*</sup>), as well as the electrons. Atomic N, N<sup>+</sup>, and N<sub>3</sub><sup>+</sup> ions are not taken into account because they play a minor role in the plasma.<sup>42</sup> Other impurities, related to oxygen or hydrogen, are also not included, although OH and O (I) emissions were also observed in ref 20 but at a lower intensity. In later work, we plan to extend the number of plasma species to provide a more detailed picture of the plasma chemistry.

(42) Martens, T.; Bogaerts, A.; Brok, W. J. M.; van Dijk, J. *Appl. Phys. Lett.* **2008**, *92*, 041504.



The reactions considered in the model are presented in Table 1 as well as their rate coefficients and the references where these data are adopted from. For the electron induced reactions, energy dependent cross sections are used. In order to include the electron energy loss associated with the rotational and vibrational excitation of N<sub>2</sub>, we included excitations to a rotational level at 0.02 eV and to two vibrational levels at 0.29 and 0.291 eV as additional energy loss terms in the electron energy continuity equation.

**Description of the Fluid Model.** The fluid model is based on solving a continuity equation (with different production and loss processes) (eq 1) as well as a transport equation (based on diffusion and migration in the electric field, for the charged species) (eq 2) for all the species:

$$\frac{\partial n_i}{\partial t} + \nabla \cdot \mathbf{J}_i = S_i \quad (1)$$

$$\mathbf{J}_i = \pm \mu_i n_i \mathbf{E} - D_i \nabla n_i \quad (2)$$

In these equations,  $n_i$  and  $\mathbf{J}_i$  stand for the densities and fluxes of species  $i$ ,  $S_i$  represents the net production rate, determined by different production and loss terms, as given by the reactions in Table 1. As mentioned above, the flux term is defined by the drift–diffusion approximation.  $D_i$  and  $\mu_i$  are the species diffusion coefficients and mobilities, respectively, and  $\mathbf{E}$  represents the instantaneous electric field. The (+)-sign in the first term of eq 2 applies to the positive ions, whereas the (–)-sign corresponds to negative ions and electrons.

Besides these two equations for every type of species, an energy conservation equation was solved for the electrons (eq 3):

$$\frac{\partial w_e}{\partial t} + \nabla \cdot \mathbf{J}_{w_e} = -e \mathbf{J}_e \cdot \mathbf{E} + S_{w_e} \quad (3)$$

$w_e$  is the electron energy density, defined as  $w_e = n_e \bar{\epsilon}$ , with  $\bar{\epsilon}$  the mean electron energy.  $\mathbf{J}_{w_e}$  is the electron energy density flux:

$$\mathbf{J}_{w_e} = -\frac{5}{3} \mu_e w_e \mathbf{E} - \frac{5}{3} D_e \nabla w_e$$

Further,  $S_{w_e}$  is the source term of the electron energy density representing the loss and gain of the electron energy due to collisions. The first term on the right-hand side of eq 3 accounts for the Ohmic heating of the electrons due to the electric field. For the other, so-called heavy particles, no energy conservation equation needs to be solved because these species can be considered more or less in thermal equilibrium with the background gas.

These equations were solved together with the Poisson equation in order to obtain a self-consistent electric field distribution (eq 4):

$$\nabla \cdot (\epsilon \mathbf{E}) = \rho \quad (4)$$

where  $\epsilon$  is the permittivity of the plasma and  $\rho$  is the space charge density obtained from the ion and electron densities.

The fluid model applied for this study forms part of the PLASIMO modeling framework developed at Eindhoven University.<sup>43</sup> The electron impact reaction rate coefficients as well as the electron mobility were described as parameters dependent on the mean electron energy. These dependencies were calculated with the BOLSIG+ Boltzmann solver,<sup>44</sup> which provides reference tables for the electron mobility and the reaction rate coefficients as a function of the mean electron energy. During the calculations, the mean electron energy was calculated from eq 3, and this energy directly determines the value of the electron mobility and reaction rate coefficients. For the ions, the local field approximation was used and mobilities were adopted from refs 45–47. The diffusion coefficients of the ions and electrons were calculated from their mobilities using the Einstein relation. For the neutral species, experimental diffusion coefficients were used, adopted from ref 48.

The boundary conditions for the equations were described using flux expressions. At the sides where there is no electrode or insulating tube present, homogeneous Neumann boundary conditions were employed, meaning that the derivative of the quantities in the direction perpendicular to these boundaries were assumed to be zero. At the sides where there is an electrode or an insulator present, the flux expressions were determined by zero densities for ions and excited species due to neutralization and de-excitation, respectively. For the electrons, the boundary condition was mainly determined by secondary electron emission from the ions using a secondary electron emission coefficient of 0.092 for the helium ions and 0.01 for the nitrogen ions. The coefficients were chosen as such to match the experimental discharge current measured in ref 20.

The coupled differential equations were solved by the so-called “modified strongly implicit method”<sup>49</sup> using an extra stabilization method, as explained in ref 50 until convergence was reached.

**Description of the Monte Carlo (MC) Model for the Electrons.** As mentioned above, we have also developed a MC model for the electrons to describe their behavior in more detail, as they are not really in equilibrium with the electric field. The MC model is based on following the behavior of a large number of individual electrons. It is not possible to follow all electrons in the plasma within a reasonable time scale because of the typical number densities of 10<sup>18</sup> electrons per m<sup>3</sup>; see below. Therefore, the real electrons were replaced by so-called superelectrons, which represent a fixed number of real electrons as defined by their weight. Typically, around 10<sup>5</sup> superelectrons are followed to obtain good statistics.

The behavior of these superelectrons was described, one after the other, as a function of time. During successive time steps,

(43) See <http://plasimo.phys.tue.nl>.

(44) Hagelaar, G. J. M.; Pitchford, L. C. *Plasma Sources Sci. Technol.* **2005**, *14*, 722–733.

(45) Ellis, H. W.; Pai, R. Y.; McDaniel, E. W.; Mason, E. A.; Viehland, L. A. *At. Data Nucl. Data Tables* **1976**, *17*, 177–210.

(46) McFarland, M.; Albritton, D. L.; Fehsenfeld, F. C.; Ferguson, E. E.; Schmeltekopf, A. L. *J. Chem. Phys.* **1973**, *59*, 6610–6619.

(47) Viehland, L. A.; Mason, E. A. *At. Data Nucl. Data Tables* **1995**, *60*, 37–95.

(48) Grigor'ev, I. S.; Meilikhov, E. Z. *Handbook of Physical Quantities*; CRC: Boca Raton, FL, 1997.

(49) Schneider, G. E.; Zedan, M. *Numer. Heat Transfer* **1981**, *4*, 1–19.

(50) Hagelaar G. Modeling of Microdischarges for Display Technology. Ph.D. Dissertation, Eindhoven University of Technology, Eindhoven, The Netherlands, 2000.

their trajectory under the influence of the electric field in the plasma was calculated by solving Newton's laws. The probability for a collision during that time step,  $\text{Prob}_{\text{coll}}$ , was calculated with eq 5 and compared with a random number between 0 and 1:

$$\text{Prob}_{\text{coll}} = 1 - \exp(-\Delta s \sum (n \sigma_{\text{coll}}(E))) \quad (5)$$

$\Delta s$  is the distance traveled during the time step, while  $n$  and  $\sigma_{\text{coll}}(E)$  are the densities of the target particles and the cross sections of the different collision types of the electrons with energy  $E$ . If the probability is lower than the random number, no collision occurs. If the probability is higher, a collision takes place and the kind of collision that takes place needs to be determined.

The collisions taken into account in the model are elastic collisions with He atoms, electron impact ionization and excitation from the He ground state atoms, and the  $\text{He}_m^*$  metastable levels. Most electron impact collisions with the  $\text{N}_2$  molecules were neglected, as these species are only present as an impurity (10 ppm). However, electron impact excitation to the lowest rotational and vibrational levels of  $\text{N}_2$  was included because it can be important to determine the electron energy distribution function in the low energy range.<sup>42,51</sup> The references where the cross sections of these processes are adopted from were presented in Table 1 above.

To determine which collision takes place, the partial collision probabilities of the various collisions were calculated based on the individual cross sections. The total collision probability, which is equal to 1 because it is the sum over all partial collision probabilities, was subdivided in intervals with lengths corresponding to these partial collision probabilities. A second random number between 0 and 1 was generated, and the interval into which the random number falls determined the collision that takes place. Then, the new energy and direction after collision were also defined by random numbers based on energy and angular differential cross sections.

This procedure of calculating the trajectory by Newton's laws and treating the collisions by random numbers was repeated during successive time steps until the superelectron was lost by recombination at the cell walls. Then, the next superelectron was followed. It should be noted that some new superelectrons can be created by ionization collisions. These additional superelectrons were also followed with the same procedure.

## RESULTS AND DISCUSSION

**Cell Geometry and Operating Conditions.** The fluid and MC model are applied to the APGD setup described in refs 19 and 20. A schematic diagram is presented in Figure 1a. The discharge chamber is a 10 cm cubic aluminum cell. The anode and cathode are located on opposite faces of the cell. The cathode is a 3 mm diameter tungsten rod with a flat, polished end surrounded by a 3 mm internal diameter and 6.35 mm outer diameter alumina tube to limit the cathode area. The anode is a cylindrical 2.5 cm diameter brass rod with a conical end with a half angle of  $60^\circ$ . The gap between the anode tip and the cathode is 1 cm. For the simulations, only the region between the anode

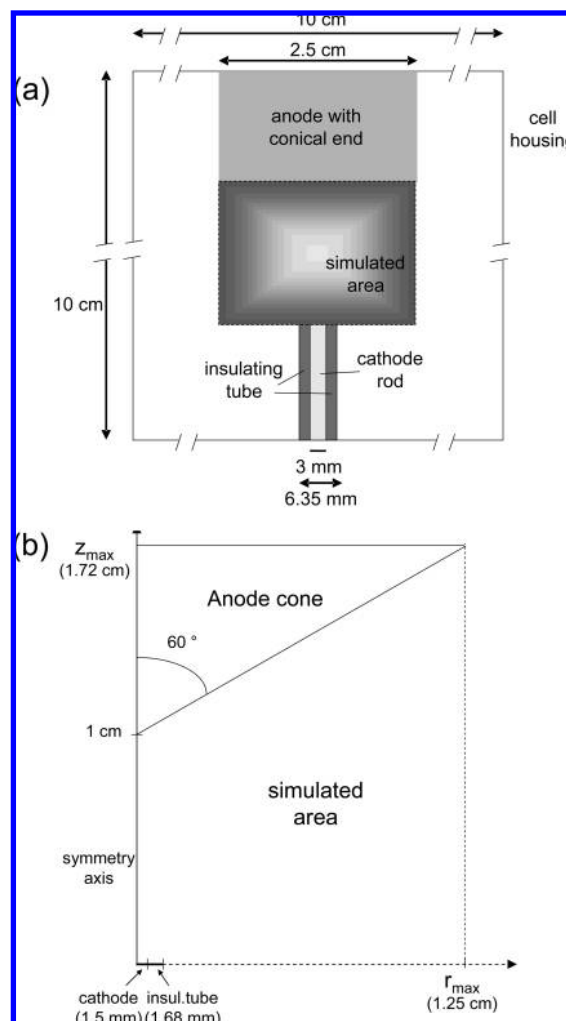


**Figure 1.** Schematic diagram of the APGD source under study (not completely to scale) (a) The shaded box gives the simulated area. Because of the cylindrical symmetry, the calculation results will be presented in only one-half of this box, as indicated in part b.

and cathode is important, where the plasma is most intense. Therefore, the calculation results will be presented only in the shaded box illustrated in Figure 1a. Moreover, because of the cylindrical symmetry of this region, only one-half of this box is sufficient to present the results because the data can be projected to the other side of the axis of symmetry. Hence, Figure 1b presents the details of the simulated area.

The calculations are performed for typical conditions of this APGD as reported in ref 20, i.e., a He pressure of 1 atm with 10 ppm of  $\text{N}_2$  as the impurity gas and a dc discharge voltage of 650 V. Secondary electron emission coefficients of 0.092 for helium ions and 0.01 for nitrogen ions and a gas temperature of 1350 K<sup>20</sup> are assumed. These conditions provide for a discharge current of 30 mA, which is also obtained in the experiments.<sup>20</sup>

**Potential and Electric Field Distributions.** Figure 2 illustrates the calculated potential distribution (part a) and (axial and radial) electric field distributions (parts b and c) in one-half of the cell as calculated with the fluid model. The cathode is found at the left end of the figure ( $z = 0$  cm), whereas the anode cone is at the right. The symmetry axis is at  $r = 0$  cm. As can be

(51) Brok, W. J. M.; Bowden, M. D.; van Dijk, J.; van der Mullen, J. J. A. M.; Kroesen, G. M. W. *J. Appl. Phys.* **2005**, *98*, 013302.

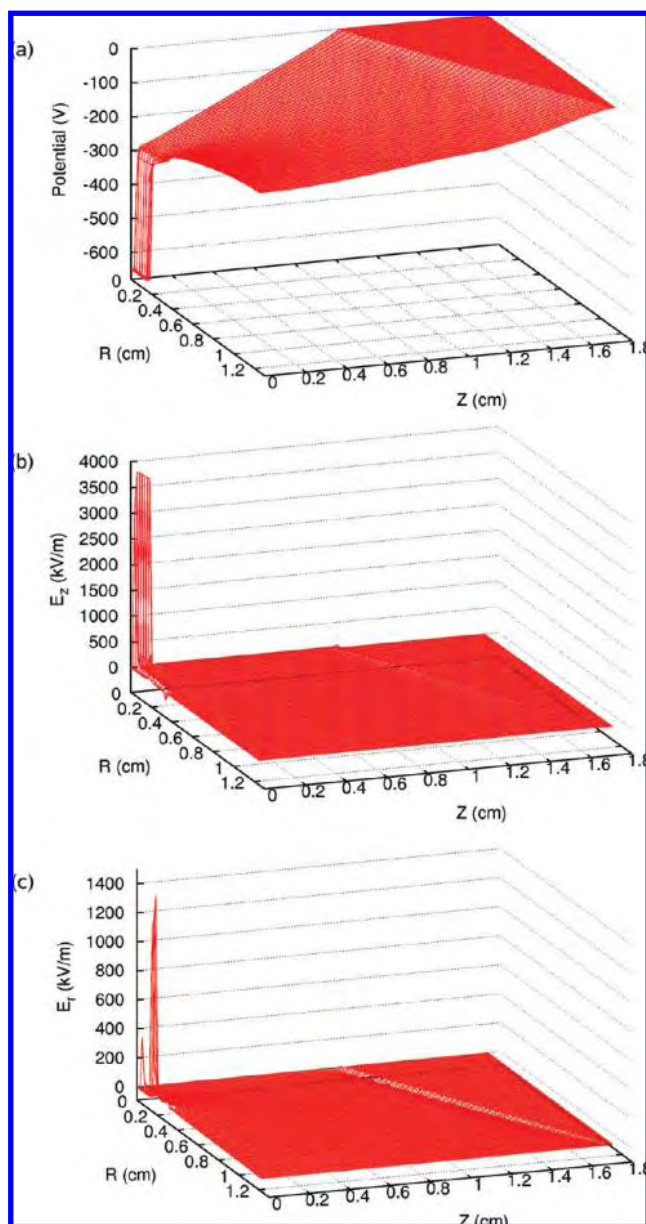


**Figure 2.** Calculated 2D electric potential distribution (a) and axial (b) and radial (c) electric field distributions in the cell geometry illustrated in Figure 1b. The cathode is found at the left ( $z = 0$ ) whereas the anode cone is at the right. The symmetry axis is at  $r = 0$ .

observed from Figure 2a, the potential drops very quickly from  $-650$  V at the cathode to about  $-300$  V at a distance of  $0.25$  mm from the cathode. This small region can be seen as the cathode dark space (CDS) region. It is much thinner than the CDS in reduced pressure GDs, where typical values of a  $0.5$ – $5$  mm are reported for pressures in the range of  $50$ – $700$  Pa.<sup>52–54</sup> However, it is in the same range as the CDS width of  $0.2$  mm calculated for a needle cathode in atmospheric pressure helium<sup>51</sup> and a CDS width of  $0.4$  mm calculated for a DBD operating in the same gas.<sup>30</sup> This is logical because it is generally known that the CDS thickness drops with increasing pressure.<sup>52</sup>

Another difference with reduced pressure GDs is the behavior of the potential in the rest of the discharge. Indeed, in the present case, the potential remains negative in the entire discharge region and it increases only gradually from  $-300$  V at the end of the CDS to zero at the anode. This is completely different from the reduced pressure case, where the potential is slightly positive (typically a few up to  $10$  V) and almost constant in the largest part of the discharge (i.e., the so-called negative glow (NG) region) before it returns to zero at the anode.<sup>53,54</sup> Such a NG region is not clearly observed in the atmospheric pressure case. Therefore, we can conclude that the APGD consists of a small CDS and a large positive column (PC), which fills most of the discharge region, whereas this PC is typically absent in reduced pressure GDs used for analytical spectrometry.<sup>39,53</sup> It is indeed generally accepted that with increasing pressure (or larger distance between anode and cathode) a PC is formed and can become the largest region in the discharge.<sup>55,56</sup> Hietje and co-workers have also clearly demonstrated by means of photography the growing importance of the PC region in the APGD under study here when raising the pressure from a few Torr to atmospheric pressure.<sup>20</sup> The presence of a PC is also observed in other publications on APGDs.<sup>29–31,38</sup>

The potential distribution presented in Figure 2a gives rise to an axial and radial electric field distribution illustrated in parts b and c of Figure 2, respectively. In the CDS, the axial electric field is  $3.8 \times 10^6$  V/m, which was also found by Shi and Kong for similar conditions in a parallel plate setup,<sup>38</sup> and it is about 2–3 times higher than the obtained values for atmospheric pressure DBDs of  $1.1$ – $1.8 \times 10^6$  V/m.<sup>29,30</sup> The calculated value is about 5 times higher than the reduced pressure GD value of about  $8 \times 10^5$  V/m obtained for both dc and pulsed dc discharges.<sup>57,58</sup> However, it remains high (i.e., in the order of  $3 \times 10^4$  V/m) in most of the discharge region, which is different from the reduced pressure GD situation. It points out the importance of the PC region, i.e., to ensure a sufficient flux of electrons toward the anode by accelerating them in the electric field and hence to maintain the electrical current throughout the discharge.<sup>55,59</sup> Indeed, it appears that at atmospheric pressure, the electrons lose so much of their energy by collisions that they would not be able to reach the anode unless they are accelerated by this electric field in the PC region. The radial electric field is presented in Figure 2c. It is very localized next to the alumina tube with values slightly above  $10^6$  V/m. Since the alumina tube is charged by the plasma also in the radial direction, a rather strong electric field is formed. The radial field is not so important since there is no electrode in this direction, and the distance to the wall of the discharge cell is  $5$  cm.

**Mean Electron Energy.** The mean electron energy, as calculated with the MC model, is plotted in Figure 3, again in one-half of the cylindrically symmetrical discharge region. In the CDS, the electrons gain a lot of energy from the electric field,

(52) Bogaerts, A.; Gijbels, R. *J. Appl. Phys.* **1995**, *78*, 6427–6431.

(53) Bogaerts, A.; Gijbels, R.; Goedheer, W. J. *Anal. Chem.* **1996**, *68*, 2296–2303.

(54) Bogaerts, A.; Gijbels, R. *Spectrochim. Acta, Part B* **1998**, *53*, 437–462.

(55) Francis, G. In *Handbuch der Physik*, Vol. 22; Flügge, S., Eds.; Springer-Verlag: Berlin, Germany, 1956.

(56) Chapman, B. *Glow Discharge Processes*; John Wiley and Sons, Ltd.: New York, 1980.

(57) Graves, D. B.; Jensen, K. F. *IEEE Trans. Plasma Sci.* **1986**, *14*, 78–91.

(58) Kutasi, K.; Hartmann, P.; Donkó, Z. *J. Phys. D: Appl. Phys.* **2001**, *34*, 3368–3377.

(59) Bogaerts, A. Mathematical Modeling of a Direct Current Glow Discharge in Argon. Ph.D. Dissertation, University of Antwerp, Wilrijk, Belgium, 1996.



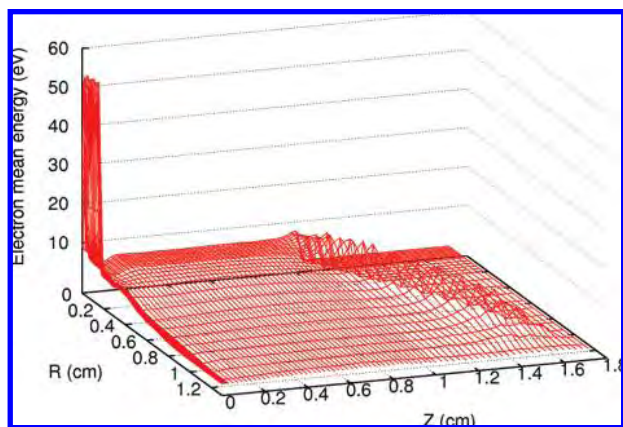


**Figure 3.** Calculated 2D profile of the mean electron energy.

but they also lose most of this energy again by inelastic collisions (i.e., ionization and excitation of the He gas). Therefore, their mean energy is only in the order of 50 eV. This is considerably lower than in reduced pressure GDs, where the mean electron energy at the end of the CDS can be as high as 500–800 eV (for 1000–1200 V discharge voltage, depending on the pressure).<sup>53,54</sup> This difference is of course explained by the fact that at low pressure the electrons do not lose so much energy by collisions.

However, because of the significant axial electric field in the PC region, the mean electron energy remains considerable (i.e., about 6 eV) in the largest part of the discharge and it increases again to almost 10 eV at the anode cone. These results are very similar to the results obtained by Shi and Kong for a dc parallel plate setup in atmospheric pressure helium.<sup>38</sup> In their work, a mean electron energy of 40 eV at the cathode is obtained together with a bulk energy of about 10 eV as well as a small increase at the anode reaching 15 eV. This profile has important consequences for the electron impact collision rates, as will be illustrated below.

**Electron Impact Collision Rates.** Figure 4 presents the two-dimensional (2D) distributions of the electron impact collision rates as obtained from the MC calculations. The wire surfaces present the data on a linear scale, while the flat surfaces in the plane of the  $R$  and  $Z$  axes present the data on a logarithmic scale. In this way, an estimate of the order of magnitude of the bulk values can be given. Light tints represent low values and dark tints represent high values. Figure 4a illustrates that the mean electron energy is only sufficient to produce ionization from the He ground state atoms in the CDS region. Indeed, this process requires 24.6 eV. This is in the range of the mean electron energy calculated at the end of the CDS but is much higher than the mean electron energy of 10 eV in the PC. However, the logarithmic scale demonstrates that the calculated ionization rate in the PC is not zero. This is because the electrons are characterized by an energy distribution with a tail ranging to much higher energies, and the latter can give rise to these inelastic collisions. The electron impact ionization rate reaches a peak of almost  $4 \times 10^{26} \text{ m}^{-3} \text{ s}^{-1}$ , which is several orders of magnitude higher than the ionization rates obtained in reduced pressure GDs, typically in the order of  $10^{22}–10^{23} \text{ m}^{-3} \text{ s}^{-1}$ .<sup>53</sup> However, it is still about 4

orders of magnitude below the ionization rates reported for a dc APGD in  $\text{H}_2$ <sup>60</sup> in a rod to plane setup.

These high localized ionization rates are again due to the atmospheric pressure, giving rise to many collisions until the energy becomes too low for ionization, which occurs already at the end of the CDS. This is important because it prevents an ionizing cascade, which would lead to an arc as is also discussed in ref 20. Integrated over the entire discharge region, the overall ionization rate of He will therefore be quite moderate.

The rate of electron impact excitation (Figure 4b) also reaches a maximum at the end of the CDS (or the beginning of the NG), but in contrast to the electron impact ionization rate, it is clearly nonzero in the region between the cathode and anode, with again a small peak near the anode tip. This is explained by the increase in mean electron energy as was anticipated above. Note that Figure 4b presents the electron impact excitation rate to the  $\text{He}_m^*$  metastable levels. The maximum value appears to be comparable to the maximum in the electron impact ionization rate. However, the total electron impact excitation rate from the He ground state atoms is about twice as high as the excitation rate to the  $\text{He}_m^*$  metastable levels as it includes also excitation to all other levels. It is not shown here because it looks qualitatively very similar to Figure 4b, with a pronounced maximum in the CDS, small but nonzero values in the region between cathode and anode, and a second maximum near the anode tip. The reason that the total excitation rate is twice as high as the ionization rate, in spite of the fact that the cross section is lower,<sup>61</sup> is due to the lower threshold for excitation compared to ionization (i.e., 19.8 vs 24.6 eV). This also explains the nonzero values in the region between the cathode and anode on the linear scale and the small maximum near the anode tip.

Finally, it should be noted that the most significant contributions in the excitation rate (visible on the linear scale) occur only for a radial position up to about 2.5 mm from the cell axis. This corresponds to the radius of the cathode and some part of the insulating tube around the cathode (cf. Figure 1). Indeed, when the electrons are emitted from the cathode, they can move slightly in the radial direction, away from the discharge center, but mostly they are accelerated in the forward direction by the axial electric field. Therefore, there are not many electrons present at radial distances further than 2 mm from the discharge axis and, consequently, not many electron impact collisions will occur in this region.

The calculated electron impact excitation rate profile is in excellent agreement with the spatial distribution of HeI lines as measured by Hieftje and co-workers,<sup>20</sup> which exhibit also a pronounced peak near the cathode, very low values in the gap between the cathode and anode, and a second, smaller maximum near the anode. Moreover, our calculation results compare favorably with the photographs taken of the APGD.<sup>20</sup> Indeed, Hieftje and co-workers observed a very bright thin layer on the cathode surface (called the NG), followed by a small dark region (the Faraday dark space or FDS), and a very diffuse cylinder of light, corresponding to the PC region, with a diameter slightly larger than the cathode diameter and with the maximum intensity close to the anode.<sup>20</sup> This is exactly what is predicted with our

(60) Farouk, T.; Farouk, B.; Staack, D.; Gutsol, A.; Fridman, A. *Plasma Sources Sci. Technol.* **2007**, *16*, 619–634.

(61) Bogaerts, A.; Gijbels, R. *J. Appl. Phys.* **2002**, *92*, 6408–6422.



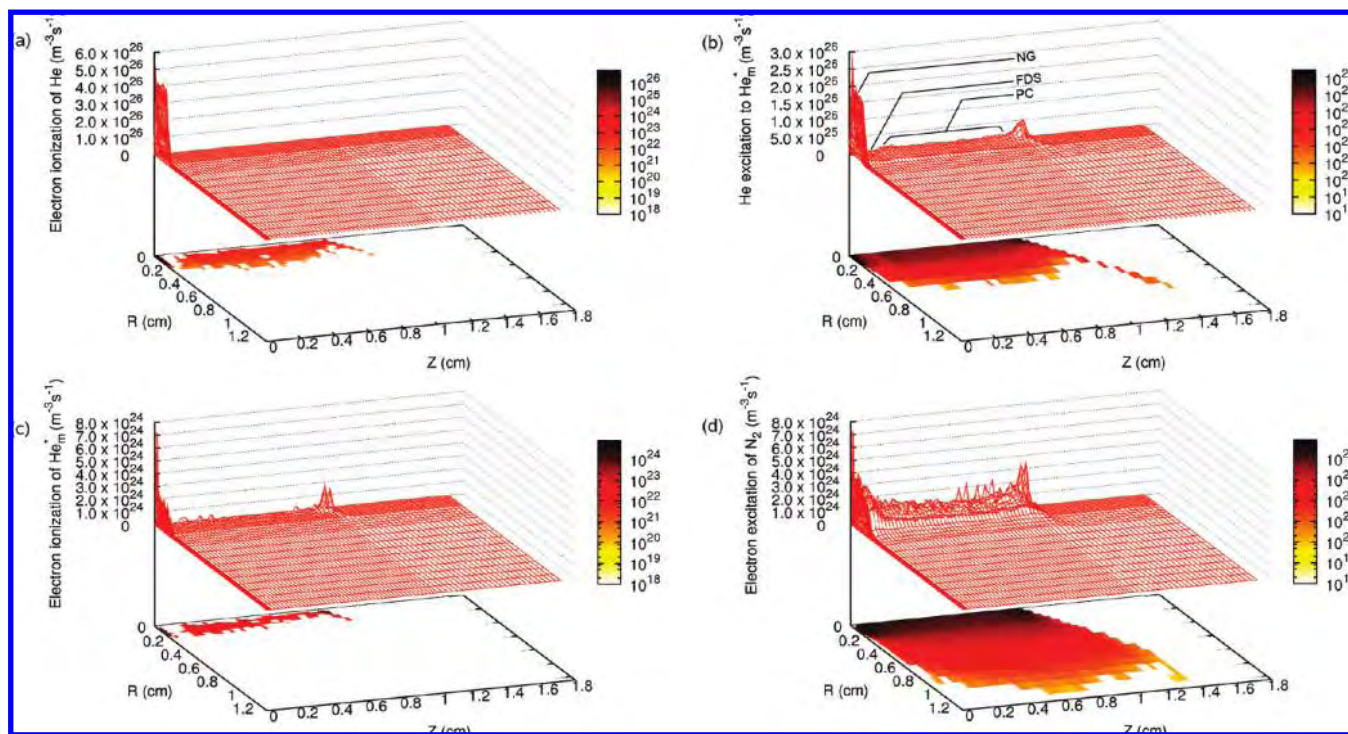


**Figure 4.** Calculated 2D profiles of the electron impact collision rates: (a) ionization of He ground state atoms, (b) excitation to the  $\text{He}_m^*$  metastable atoms, (c) ionization from the  $\text{He}_m^*$  metastable atoms, and (d) rotational–vibrational excitation of the  $\text{N}_2$  molecules. In part b, different spatial zones of the GD, as obtained from the excitation (or emission) intensities, are also schematically indicated.

MC simulations presented in Figure 4b. The different spatial zones are therefore also schematically indicated in this figure.

Although electron impact ionization from the He ground state atoms is found to be almost negligible in the largest part of the discharge, ionization from the  $\text{He}_m^*$  metastable atoms appears to be possible in the region between the cathode and anode and especially near the anode tip, as is clear from Figure 4c. Indeed, a much lower amount of energy is required to ionize the  $\text{He}_m^*$  metastable levels, as they are already excited to 19.8 eV. Hence, only 4.8 eV is needed to ionize them, compared to 24.6 eV for ionization of the He ground state atoms. Comparing the absolute values of parts a and c of Figure 4 tells us that the ionization rate from the  $\text{He}_m^*$  metastable levels is almost 2 orders of magnitude lower than ionization from the He ground state. Nevertheless, this illustrates again that ionization from the  $\text{He}_m^*$  metastable levels is more efficient (due to the lower energy threshold) because the  $\text{He}_m^*$  metastable atom density is more than 5 orders of magnitude lower than the He background gas density (see below, Plasma Species Number Densities).

Finally, Figure 4d illustrates the rate of rotational and vibrational excitation of the  $\text{N}_2$  gas. We included excitations to one rotational level at 0.02 eV and to two vibrational levels at 0.29 and 0.291 eV as additional energy loss processes. Note that the  $\text{N}_2$  density is also 5 orders of magnitude lower than the He density, at an impurity level of 10 ppm, and hence comparable to the  $\text{He}_m^*$  density. Nevertheless, the rate of rotational and vibrational excitation of the  $\text{N}_2$  gas is considerable because the cross section reaches a maximum between 1 and 5 eV, which is close to the mean electron energy in the discharge (cf. Figure 3). This process is important as it determines the electron energy distribution function in the lower

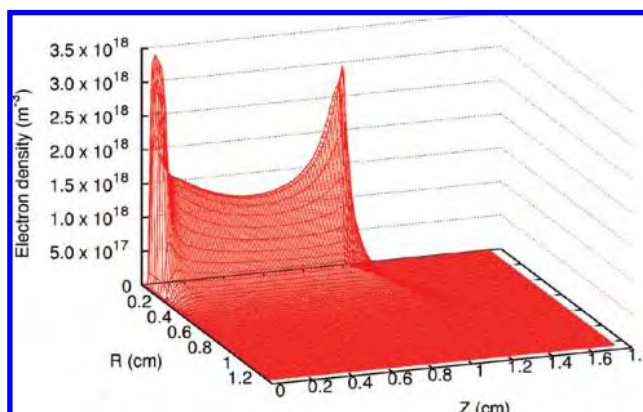


**Figure 5.** Calculated 2D electron number density profile.

energy region, where the other inelastic processes with He (ionization, excitation) do not occur. Indeed, the threshold for rotational and vibrational excitation is assumed to be 0.02 eV, which is significantly lower than the threshold for ionization and excitation of He (i.e., 24.6 and 19.8 eV, respectively).

**Plasma Species Number Densities.** The 2D electron number density profile is plotted in Figure 5. The results shown here were obtained with the fluid model, but the MC simulations yielded almost exactly the same profile, which can be considered as a validation of both models. The electron density reaches a maximum of about  $3.5 \times 10^{18} \text{ m}^{-3}$  at a distance of 0.35 mm from the cathode, which corresponds to the end of the CDS region. This is quite similar to low pressure GDs, although in that case a much broader maximum is observed, which fills most of the NG region.<sup>53,54</sup> Indeed, in the present case, the density drops quickly by about a factor of 2 and maintains values of about  $1.4 \times 10^{18} \text{ m}^{-3}$  throughout the gap between the cathode and anode,

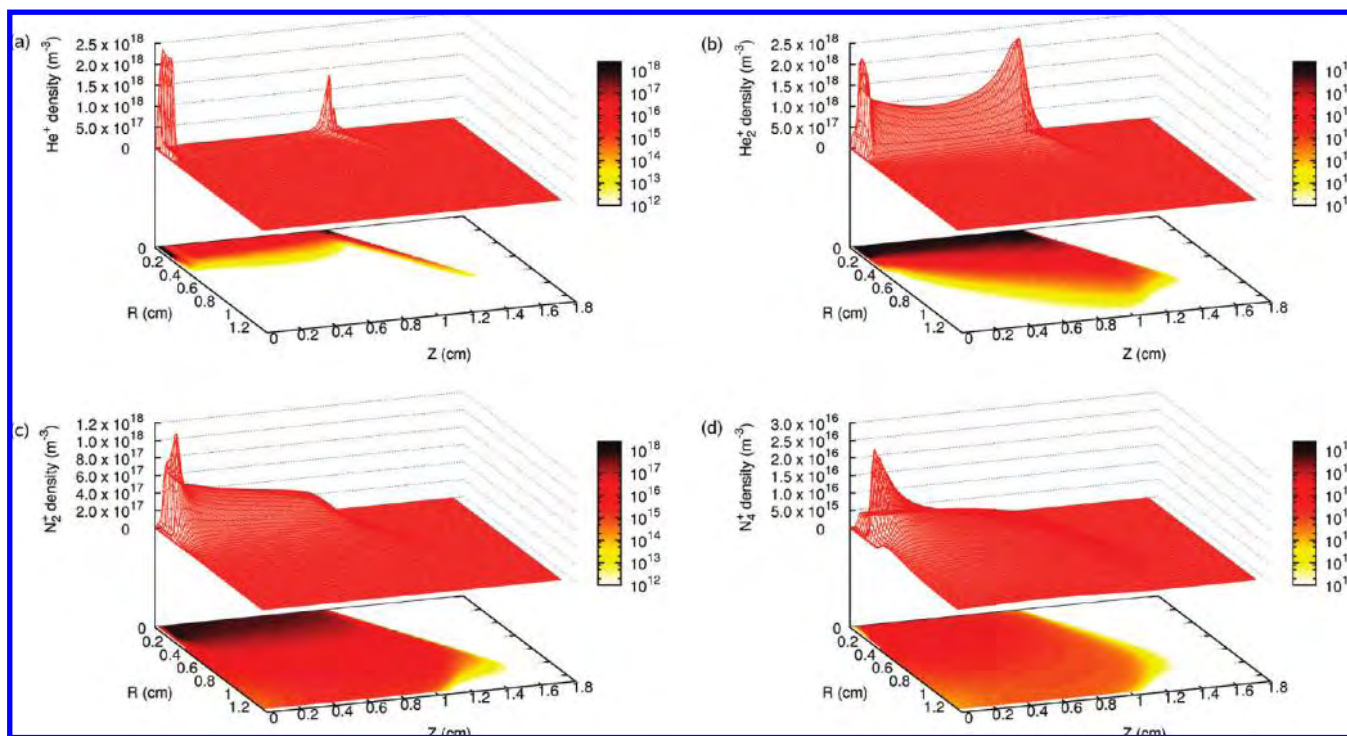


**Figure 6.** Calculated 2D number density profiles of the  $\text{He}^+$  (a),  $\text{He}_2^+$  (b),  $\text{N}_2^+$  (c), and  $\text{N}_4^+$  (d) ions.

until it increases again to values around  $3 \times 10^{18} \text{ m}^{-3}$  near the anode cone (i.e., at the end of the PC region). As was anticipated above, the density becomes negligible at radial distances further than 2.5 mm from the discharge axis because the electrons emitted from the cathode are mainly accelerated in the forward direction. The two maxima in the electron number density profile correspond to the two maxima in the electron impact ionization rate (at least for ionization from the  $\text{He}_m^*$  metastable levels) and are characteristic for an APGD, where the PC region plays an important role.

We believe that this second maximum in electron density and in electron impact ionization and excitation rates is partly induced by the conical end of the anode rod. Indeed, Figure 2a demonstrated two important effects that influence the electrons. The cone shaped end with a half angle of  $60^\circ$  creates an active region where the distance between the electrodes decreases and consequently the electric field slightly increases. In this way a funnel-like potential distribution is created, as can be seen in Figure 2a, which confines the discharge toward the axis of symmetry of the setup and can be an important effect to maintain and stabilize the discharge. The second effect is the already mentioned potential gradient in the PC region. While in reduced pressure GDs the electrical potential in the plasma bulk is often slightly positive without any gradient, in this APGD setup there is clearly still a potential gradient in the plasma bulk. This provides for a weak electric field that pushes the electrons toward the anode. Since there is no strong electric field at that location, a population of electrons with rather low energies is accumulated, as can be seen in Figure 3. Hence, there is a significant population of electrons near the anode in order to ionize the  $\text{He}_m^*$  metastable levels, but the population of electrons with enough energy to ionize ground state He is rather small. This explains the two maxima

for the ionization rate of  $\text{He}_m^*$  and the single maximum for the ionization rate of ground state He.

Comparing the absolute values of the electron number density between the APGD and reduced pressure GDs (where values of  $10^{17}$ – $10^{20} \text{ m}^{-3}$  are commonly reported<sup>53,54</sup>) tells us that the electron density is in the same order of magnitude, in spite of the higher gas pressure in the APGD. From the ideal gas law, the He background gas density at 1 atm and 1350 K can be estimated in the order of  $10^{25} \text{ m}^{-3}$ . This indicates that the ionization degree in the APGD is very low, i.e., in the order of  $10^{-7}$  (compared to  $10^{-5}$ – $10^{-3}$  for reduced pressure GDs<sup>54,62</sup>).

Figure 6 presents the 2D number density profiles of the various ions in the plasma. The  $\text{He}^+$  density (Figure 6a) reaches a pronounced maximum of  $2.3 \times 10^{18} \text{ m}^{-3}$  near the cathode and a second maximum of about  $10^{18} \text{ m}^{-3}$  near the anode tip, but in between, the density is virtually zero in most of the plasma region. This is different from the  $\text{He}_2^+$  density (Figure 6b), which exhibits also two maxima in the same order of magnitude as the  $\text{He}^+$  density, but the second maximum is clearly higher (up to  $2.5 \times 10^{18} \text{ m}^{-3}$ ) and broader, and more importantly, the density does not drop to zero in between these maxima but remains in the order of  $10^{18} \text{ m}^{-3}$  throughout the discharge, at least for radial distances up to 2.5 mm from the discharge axis. Therefore, the  $\text{He}_2^+$  density is characterized by a similar profile as the electron density (cf. Figure 5).

Hence, from parts a and b of Figure 6, it can be concluded that the  $\text{He}_2^+$  ions are present at a higher density in the plasma than the  $\text{He}^+$  ions. At first sight, this might be a bit unexpected, as the  $\text{He}^+$  ions are directly formed by electron impact ionization from the He background gas, whereas the  $\text{He}_2^+$  ions can only be formed by secondary reactions (i.e., reactions 7,

(62) Bogaerts, A.; Gijbels, R. *Anal. Chem.* **1996**, *68*, 2676–2685.



14, and 17 of Table 1; see also Production and Loss Processes of the Plasma Species). Nevertheless, it is quite common in APGDs that the molecular ions are more important than the atomic ions.<sup>42,63,64</sup>

Parts c and d of Figure 6 illustrate the  $N_2^+$  and  $N_4^+$  number density profiles. These ions are not characterized by a second maximum near the anode, but the first maximum near the cathode is followed by a gradual decrease in density throughout the discharge. It is also apparent from these figures that the maximum is shifted slightly off-axis. Comparing the absolute values tells us that the  $N_2^+$  ion density is only slightly lower than the  $He^+$  and  $He_2^+$  densities, in spite of the fact that the  $N_2$  gas density is 5 orders of magnitude lower than the He gas density. This is because the  $N_2^+$  ions are easily produced by secondary reactions (i.e., reactions 8, 11, 12, 15, and 18 from Table 1), as will also be explained later. Hieftje and co-workers also observed intense emission from the APGD attributed to  $N_2^+$  bands.<sup>20</sup> For the  $N_4^+$  ions, on the other hand, our calculations predict a density about 2 orders of magnitude lower than the other ion densities and, hence, it does not really contribute to the space charge.

In a previous paper, we have investigated the effect of  $N_2$  impurities in a He DBD.<sup>42</sup> It was demonstrated that the  $He^+$  ions were negligible for all  $N_2$  impurity levels investigated (0–2000 ppm). The  $He_2^+$  ions were only dominant for impurity levels below 1 ppm. In the region between 1 and 17 ppm of  $N_2$ , the  $N_2^+$  ions appeared to have the highest density, whereas for higher impurity levels, the  $N_4^+$  ions became predominant.<sup>42</sup> Naturally, the operating conditions were different in that study (i.e., a parallel plate DBD with a sinusoidal applied voltage of 2.6 kV amplitude and 10 kHz frequency), but it illustrates that it is indeed not so unexpected that the  $N_2^+$  (and even  $N_4^+$ ) ions can play an important role in dc powered He APGDs, even with small  $N_2$  impurity levels. To validate the calculated results for the APGD under investigation, it would be interesting to study the importance of  $N_4^+$  ions in this kind of plasma by experiments.

Comparing the  $N_2^+$  ion density with the  $N_2$  gas density (of about  $10^{20} \text{ m}^{-3}$  at 10 ppm impurity level) tells us that the ionization degree of  $N_2$  is significantly higher than the He ionization degree, i.e., in the order of  $10^{-3}$ – $10^{-2}$ . This finding is important for analytical applications because it suggests that the APGD in He can also in general efficiently ionize gaseous analytes or aerosols for detection with mass spectrometry, as is demonstrated in the papers cited in the introductory material (e.g., refs 18–22 and 26–28. In the future, we plan to include also analyte species in the model to investigate this in more detail.

Figure 7 depicts the total positive ion density (i.e., sum of all ions from Figure 6), as well as the electron density, as a function of distance from the cathode on the axis of symmetry. It is observed that the total ion density is more or less equal to the electron density so that there exists charge neutrality in most of the discharge region, except in the CDS, where only the ions are present and the electron density is virtually zero, leading to a positive space charge region. This characteristic is typical for a (reduced pressure) GD. Figure 7 explains the potential distribution on the axis of symmetry of the setup. Since the positively charged

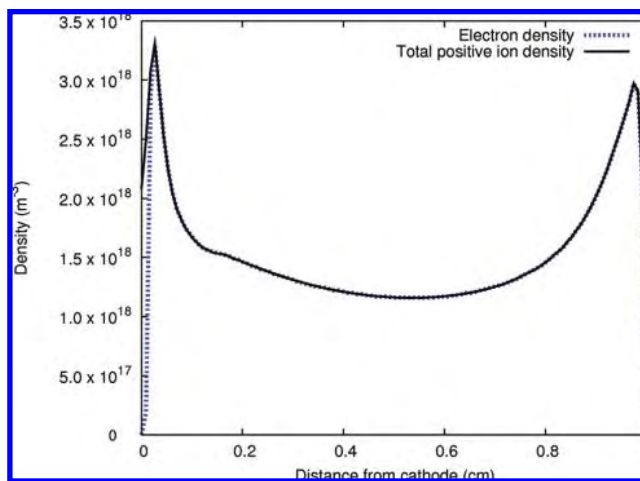


**Figure 7.** Calculated 1D profiles of the total positive ion number density (i.e., sum of  $He^+$ ,  $He_2^+$ ,  $N_2^+$ , and  $N_4^+$  ions; solid line) and electron density (dashed line) taken at the discharge axis.

sheath is very small and the region with charge neutrality is very big, the cathode potential is not able to rise up to a zero or slightly positive value. Since the rest of the discharge has charge neutrality and cannot disturb the electric field, the electric potential continues to rise linearly up to the grounded anode. These features are typical for a glow discharge. On the other hand, if we compare this result with an atmospheric pressure DBD in the Townsend regime where the total positive ion density is typically significantly higher than the electron density (even up to 2 orders of magnitude,<sup>65–67</sup> while in our case most of the discharge exhibits charge neutrality, we can conclude that the discharge under study in this article is definitely in the glow mode.

Finally, in Figure 8, the 2D density profiles of the excited He species (i.e., the  $He_m^*$  metastable atoms (part a) and the  $He_2^*$  excimers (part b)) are plotted. The  $He_m^*$  density reaches a pronounced maximum near the cathode and a second smaller maximum near the anode. It has a considerably lower density in the bulk, but this value is still quite high in the order of  $10^{19} \text{ m}^{-3}$ , as can be seen on the logarithmic scale in Figure 8a. This is in correspondence with the electron impact excitation rate (cf. Figure 4b). The  $He_2^*$  excimers are characterized by a similar profile as the electrons and  $He_2^+$  ions, with a pronounced maximum near the cathode but still fairly high values in the gap and rising again to a second (broader but smaller) maximum near the anode. The maximum in the  $He_m^*$  density is 5 orders of magnitude lower than the He gas density (which is about  $10^{25} \text{ m}^{-3}$  at 1 atm and 1350 K, see above), but the overall fraction of metastables is of course lower because the density is almost zero in the rest of the discharge, whereas the He gas density has a nearly constant density distribution. The  $He_m^*$  metastables are in the sheath clearly dominant over the excimer molecules, while in the plasma bulk their densities are of the same order, as can be seen by comparing the logarithmic surfaces of Figure 8a,b.

(63) Shon, J. W.; Kushner, M. J. *J. Appl. Phys.* **1994**, *75*, 1883–1890.

(64) Yuan, X.; Raja, L. L. *Appl. Phys. Lett.* **2002**, *81*, 814–816.

(65) Petrović, D.; Martens, T.; van Dijk, J.; Brok, W. J. M.; Bogaerts, A. *J. Phys. D: Appl. Phys.* **2009**, *42*, 205206.

(66) Massines, F.; Ségur, P.; Gherardi, N.; Khamphan, C.; Ricard, A. *Surf. Coating Technol.* **2003**, *174*, 8–14.

(67) Golubovskii, Yu. B.; Maiorov, V. A.; Li, P.; Lindmayer, M. *J. Phys. D: Appl. Phys.* **2006**, *39*, 1574–1583.

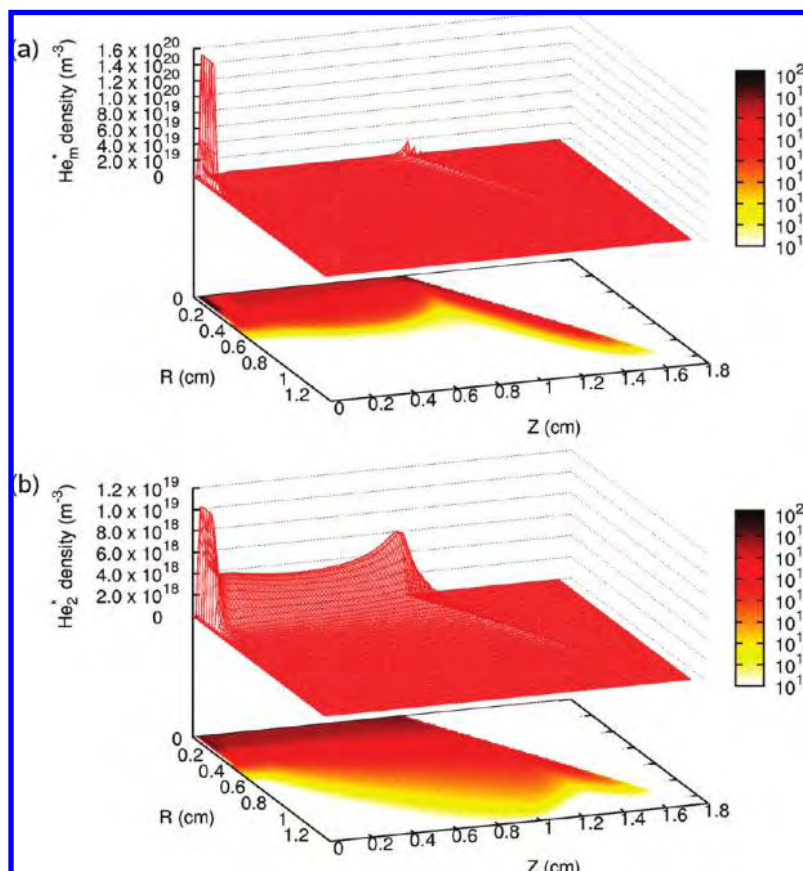


**Figure 8.** Calculated 2D number density profiles of the He<sub>m</sub>\* metastable atoms (a) and the He<sub>2</sub>\* excimers (b).

#### Production and Loss Processes of the Plasma Species.

As stated in ref 20, quantitative models for analytical APGDs have not yet been developed and the authors found it difficult to provide detailed explanations for the results they obtained, more specifically about the role of various processes and mechanisms.<sup>20</sup> For instance, it is generally established<sup>29,68</sup> that N<sub>2</sub><sup>+</sup> ions in He discharges can be formed through Penning ionization by He<sub>m</sub>\* metastable atoms as well as by asymmetric charge transfer of He<sub>2</sub><sup>+</sup> ions, but it is not possible to determine a priori which of these reactions will be dominant in the APGD under study.<sup>55</sup> Therefore, Table 2 presents the calculated relative contributions of the most important production and loss processes for the different plasma species obtained by integrating over the entire discharge region.

The He<sup>+</sup> ions are mainly formed by electron impact ionization of He ground state atoms as well as from the He<sub>m</sub>\* metastable levels. Hornbeck–Molnar ionization by collisions of two He<sub>m</sub>\* atoms contributes for about 10%. The major loss mechanism is conversion into He<sub>2</sub><sup>+</sup> ions, although electron-ion recombination (leading to either He ground state or excited atoms) also contributes for about 12%. All these production and loss rates are characterized by a maximum near the cathode and a second maximum near the anode tip but virtually zero values in between.

The He<sub>2</sub><sup>+</sup> ions are mainly created by Hornbeck–Molnar associative ionization, i.e., due to collisions of two He<sub>m</sub>\* atoms, although conversion out of He<sup>+</sup> ions is also quite important. The rate of Hornbeck–Molnar associative ionization is plotted in 2D in Figure 9a. It is clear that this rate exhibits a pronounced maximum near the cathode, but the values in the entire gap between the cathode and anode are still rather high (see logarithmic scale). This explains why the He<sub>2</sub><sup>+</sup> ions are also characterized by fairly high density values in the entire region between cathode and anode (see Figure 6b), in contrast to the He<sup>+</sup> ions (cf. Figure 6a), for which the dominant production process (i.e., electron impact ionization) showed a pronounced maximum near the cathode and was almost zero in the gap between cathode and anode (see Figure 4a,c).

The loss of He<sub>2</sub><sup>+</sup> ions is almost exclusively due to charge transfer with N<sub>2</sub>, giving rise to N<sub>2</sub><sup>+</sup> ions as appears in Table 2. This is also the dominant production mechanism for the N<sub>2</sub><sup>+</sup> ions. Other important production processes are Penning ionization of N<sub>2</sub> due to collisions with either He<sub>m</sub>\* atoms or He<sub>2</sub>\* excimers, which both contribute for roughly 10%. The rate of this dominant production process is depicted in Figure 9b. It is characterized by two (nearly equal) maxima near the cathode and the anode and fairly high values in between explaining the N<sub>2</sub><sup>+</sup> density profile shown in Figure 6c (except for the maximum near the anode, which has disappeared in the N<sub>2</sub><sup>+</sup> ion density profile as a result of the loss processes). The loss of N<sub>2</sub><sup>+</sup> ions is mainly attributed to recombination with electrons, although conversion into N<sub>4</sub><sup>+</sup> ions upon collision with He gas atoms also contributes for 11%.

(68) Anderson, C.; Hur, M.; Zhang, P.; Mangolini, L.; Kortshagen, U. J. *Appl. Phys.* **2004**, *96*, 1835–1839.

(69) Deloche, R.; Monchicourt, P.; Cheret, M.; Lambert, F. *Phys. Rev. A* **1976**, *13*, 1140–1176.

(70) Kossyi, I. A.; Kostinsky, A. Yu.; Matveyev, A. A.; Silakov, V. P. *Plasma Sources Sci. Technol.* **1992**, *1*, 207–220.

(71) Albritton, D. L. *At. Data Nucl. Data Tables* **1978**, *22*, 1–101.



**Table 2. Calculated Relative Contributions (in %) of the Production and Loss Processes for the Various Plasma Species, Taken into Account in the Model<sup>a</sup>**

He <sup>+</sup> production processes	%	He <sup>+</sup> loss processes	%
electron impact ionization from He <sup>0</sup> (2)	63	conversion into He <sub>2</sub> <sup>+</sup> (9)	88
electron impact ionization from He <sub>m</sub> <sup>*</sup> (3)	27	recombination with electrons (4,5)	12
Hornbeck–Molnar ionization from 2 He <sub>m</sub> <sup>*</sup> (16)	10		
He <sub>2</sub> <sup>+</sup> production processes	%	He <sub>2</sub> <sup>+</sup> loss processes	%
Hornbeck–Molnar associative ionization (17)	57	charge transfer with N <sub>2</sub> (10)	99.9
conversion from He <sup>+</sup> (9)	41	recombination with electrons (6)	0.1
ionization from 2 He <sub>2</sub> <sup>*</sup> (20)	2		
N <sub>2</sub> <sup>+</sup> production processes	%	N <sub>2</sub> <sup>+</sup> loss processes	%
charge transfer between He <sub>2</sub> <sup>+</sup> and N <sub>2</sub> (10)	77	recombination with electrons (7)	89
Penning ionization of N <sub>2</sub> by He <sub>m</sub> <sup>*</sup> (18)	13	conversion into N <sub>4</sub> <sup>+</sup> ions (12)	11
Penning ionization of N <sub>2</sub> by He <sub>2</sub> <sup>*</sup> (21)	9		
conversion from N <sub>4</sub> <sup>+</sup> ions (14)	2		
N <sub>4</sub> <sup>+</sup> production processes	%	N <sub>4</sub> <sup>+</sup> loss processes	%
conversion from N <sub>2</sub> <sup>+</sup> ions (12)	100	recombination with electrons (8)	81
		conversion into N <sub>2</sub> <sup>+</sup> ions (14)	19
He <sub>m</sub> <sup>*</sup> production processes	%	He <sub>m</sub> <sup>*</sup> loss processes	%
electron impact excitation (1)	99	Hornbeck–Molnar associative ionization (17)	41
electron–He <sup>+</sup> recombination (5)	1	Hornbeck–Molnar ionization (16)	24
		electron impact ionization (3)	32
		conversion into He <sub>2</sub> <sup>*</sup> (15)	2
		Penning ionization of N <sub>2</sub> (18)	1
He <sub>2</sub> <sup>*</sup> production processes	%	He <sub>2</sub> <sup>*</sup> loss processes	%
charge transfer between He <sub>2</sub> <sup>+</sup> and N <sub>2</sub> (10)	73	dissociation upon collision with third body (19)	58
conversion from He <sub>m</sub> <sup>*</sup> (15)	27	Penning ionization of N <sub>2</sub> (21)	33
			9

<sup>a</sup> The numbers in parentheses correspond to the reactions given in Table 1.

The latter process is entirely responsible for the creation of N<sub>4</sub><sup>+</sup> ions as is clear from Table 2. The rate of this process is presented in Figure 9c. It exhibits the same profile as the N<sub>2</sub><sup>+</sup> ion density and can also explain the N<sub>4</sub><sup>+</sup> ion density profile. The N<sub>4</sub><sup>+</sup> ions mainly get lost by recombination with electrons, although conversion into N<sub>2</sub><sup>+</sup> ions upon collision with He gas atoms (i.e., the opposite from the production process) also contributes for nearly 20%.

Figure 9 illustrates that not all reaction mechanisms exhibit a pronounced peak near the cathode and a smaller peak near the anode, with very low values in between (like the electron impact collision rates), but can also be characterized by fairly high values in the entire PC region. This is in qualitative agreement with emission maps presented in ref 20 for some molecular species.

As far as the excited species are concerned, the He<sub>m</sub><sup>\*</sup> metastable atoms are almost exclusively created by electron impact excitation from the ground state, whereas they get lost by several mechanisms, the most important being Hornbeck–Molnar (associative) ionization, giving rise to both He<sub>2</sub><sup>+</sup> and He<sup>+</sup> ions, as well as electron impact ionization from the metastable level.

Finally, the He<sub>2</sub><sup>\*</sup> excimers are mainly formed by charge transfer between He<sub>2</sub><sup>+</sup> ions and N<sub>2</sub> (which appeared also the dominant production process for the N<sub>2</sub><sup>+</sup> ions; see above) as

well as by conversion of He<sub>m</sub><sup>\*</sup> metastables into He<sub>2</sub><sup>\*</sup> excimers in a three-body collision with He gas atoms. The most important loss mechanisms for the He<sub>2</sub><sup>\*</sup> excimers are dissociation upon collision with a third body as well as the collision among two He<sub>2</sub><sup>\*</sup> excimers, yielding ionization of one and dissociation of the other excimer. Finally, dissociation due to the collision with N<sub>2</sub> molecules also contributes for about 10%.

## CONCLUSIONS

Fluid and MC simulations are applied to quantitatively characterize an atmospheric pressure glow discharge (APGD) in He used for analytical spectrometry. The calculation results include the potential and electric field distributions in the plasma, the density profiles of the various plasma species throughout the discharge, the mean electron energy as well as the rates of the various collision processes in the plasma, and the relative importance of the different production and loss rates for the various species. The similarities and differences with low pressure glow discharge are discussed.

From the potential distribution as well as from the electron impact excitation rate profile, the different spatial regions in the discharge can be distinguished. The positive column is dominating the discharge, in agreement with experimental observations.<sup>20</sup> Electron impact ionization is only occurring near the cathode, i.e., in the small

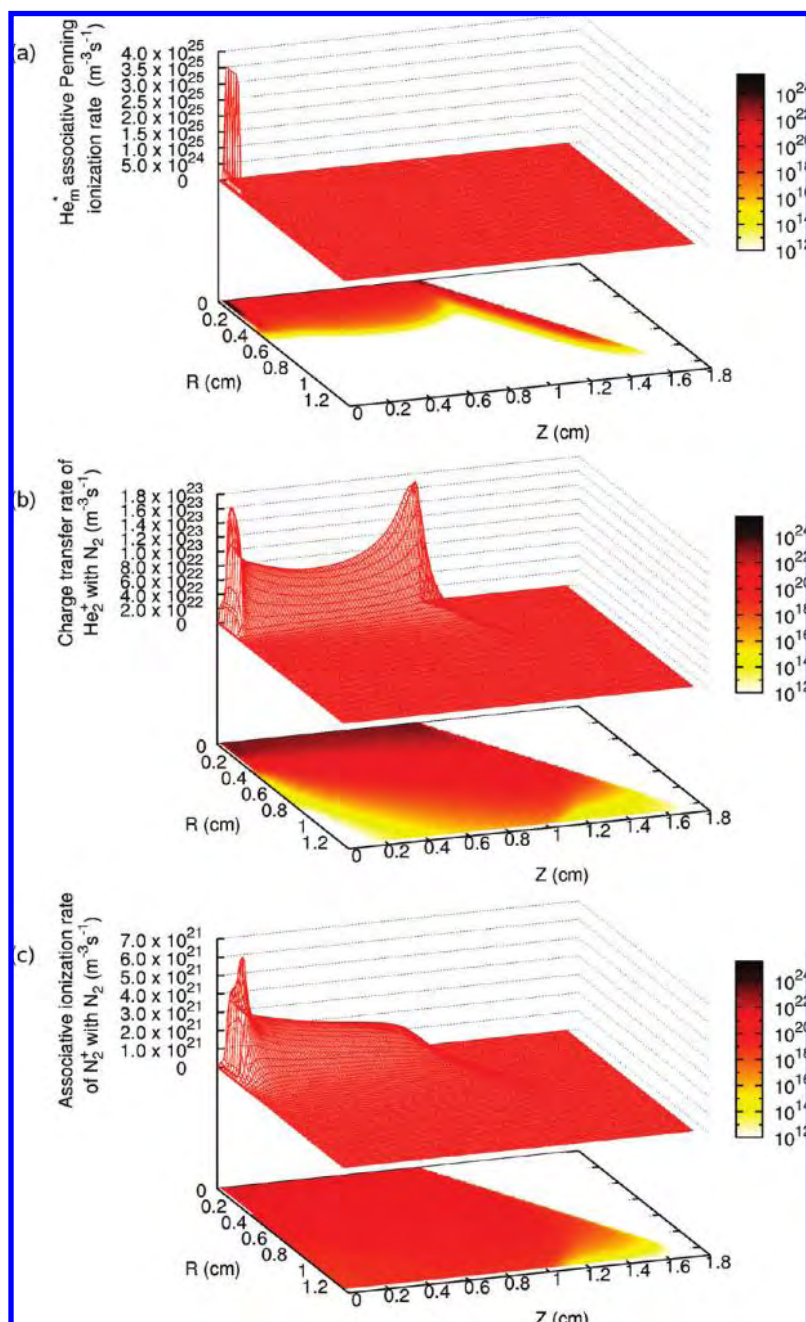


**Figure 9.** Calculated 2D reaction rate profiles of the dominant production mechanisms of (a) the  $\text{He}_m^+$  ions (i.e., Hornbeck–Molnar associative ionization), (b) the  $\text{N}_2^+$  ions and  $\text{He}_2^*$  excimers (i.e., charge transfer between  $\text{He}_2^+$  and  $\text{N}_2$ ), and (c) the  $\text{N}_4^+$  ions (i.e., conversion from  $\text{N}_2^+$  ions). The dominant production mechanisms for the  $\text{He}^+$  ions and  $\text{He}_m^*$  metastable atoms are electron impact ionization/excitation for which the rates were presented in Figure 4a,b.

CDS and NG regions, and it becomes negligible at further distances, when the electron energy has dropped to too low values. This is important to limit the amount of ionization and to prevent the transition into an arc discharge. The  $\text{He}_2^+$  ions appear to be the dominant positive ions. They are present in the entire discharge gap, in contrast to the  $\text{He}^+$  ions, which are almost only observed near the cathode and anode. The  $\text{N}_2^+$  ion density is only slightly lower than the  $\text{He}_2^+$  and  $\text{He}^+$  ion densities, in spite of the much lower  $\text{N}_2$  density (i.e., assumed to be present as impurity of 10 ppm). This indicates that  $\text{N}_2$  gas molecules are more efficiently ionized, mainly by asymmetric charge transfer of  $\text{He}_2^+$  ions as well as by Penning ionization due to  $\text{He}_m^*$  metastable atoms and  $\text{He}_2^*$  excimers. This suggests that the APGD has good potential

as an ionization source for the analysis of gaseous compounds. In future work, we would like to extend this model to describe also the flowing afterglow because of its interest for analytical spectrometry, such as ambient mass spectrometry.<sup>21,22</sup>

## ACKNOWLEDGMENT

A. Bogaerts would like to thank G. Hieftje for the interesting discussions about their APGD. The computing facility Calqua of the University of Antwerp is gratefully acknowledged.

Received for review August 6, 2009. Accepted September 24, 2009.

AC9017742